

# The self-sputtered contribution to the lunar exosphere

A. R. Poppe,<sup>1,2</sup> J. S. Halekas,<sup>1,2</sup> M. Sarantos,<sup>2,3,4</sup> and G. T. Delory<sup>1,2</sup>

Received 11 June 2013; revised 26 August 2013; accepted 31 August 2013.

[1] The lunar exosphere is produced by a combination of processes including thermal desorption, micrometeoroid bombardment, internal gas release, photon-stimulated desorption, and charged-particle sputtering. Here we investigate an additional mechanism not previously considered for the Moon, namely the role that newly born ions from the exosphere itself play in sputtering additional neutrals from the lunar surface, known as self-sputtering. Our calculations suggest that this process may sputter neutrals into the lunar exosphere at a rate equal to or greater than charged-particle sputtering due to passage through the Earth's plasma sheet when spatially averaged over the lunar dayside, while locally, self-sputtering may equal or exceed solar wind charged-particle sputtering and micrometeoroid bombardment. We use known or modeled densities and distributions of exospheric neutrals, laboratory-derived values for the photoionization rates and neutral sputtering yields, and knowledge of the ambient electromagnetic environment at the Moon to derive estimates of the self-sputtered neutral flux. We present the spatial variation of the self-sputtered neutral flux and discuss the implications thereof.

**Citation:** Poppe, A. R., J. S. Halekas, M. Sarantos, and G. T. Delory (2013), The self-sputtered contribution to the lunar exosphere, *J. Geophys. Res. Planets*, 118, doi:10.1002/jgre.20148.

## 1. Introduction

[2] The Moon possesses a tenuous, collisionless neutral exosphere believed to be composed of a broad collection of species both innate and foreign to the Moon. The exosphere is generated by a collection of processes including high-energy charged particle bombardment, micrometeoroid bombardment, photon- and electron-stimulated desorption, internal gas release, and thermal desorption [Stern, 1999]. In turn, each of these production mechanisms generates neutrals with characteristic energies, distributions, and temporal variability. Absent from this list is the production of exospheric neutrals via surface bombardment of newly born exospheric ions as they respond to the ambient electromagnetic environment, otherwise known as “self-sputtering.” Self-sputtering has been proposed to operate at Mercury [Leblanc *et al.*, 2003; Killen *et al.*, 2004; Würz *et al.*, 2010] and the satellites of the outer planets, such as Europa [Ip, 1996; Ip *et al.*, 1998]; however, such a calculation has not been performed for the Moon despite a plethora of observations of lunar exospheric pickup ions [Mall *et al.*, 1998; Yokota *et al.*, 2009; Tanaka *et al.*, 2009; Wang *et al.*, 2011;

Halekas *et al.*, 2012, 2013; Poppe *et al.*, 2012b]. Self-sputtering fluxes depend on the density and distribution of neutrals in the exosphere, the photoionization rates as a function of species and solar conditions, and the ambient electromagnetic environment which serves under certain conditions at the Moon to accelerate newly born ions up to and above keV energies. At these energies, the neutral sputtering yield of heavy ions ( $m > 4$  amu) ranges from 1 to 3 orders of magnitude greater than the sputtering yield of protons [Biersack and Eckstein, 1984; Behrisch and Eckstein, 2007]. Thus, even though the ambient exospheric neutral densities are relatively low, the combination with high sputtering yields could provide a significant generation mechanism of additional exospheric neutrals.

[3] In order to calculate the self-sputtered neutral flux at the Moon, we must assemble three components: (1) the densities and distributions of the various neutral constituents of the lunar exosphere, based either on previous measurements, upper limits, or model-based estimates; (2) the flux and differential energy distribution of ions impacting the lunar surface as a function of the ion species and the relevant ambient plasma parameters; and (3) the neutral sputtering yield as a function of ion mass and impact energy. Section 2 describes each of these components followed by a calculation of the total neutral self-sputtered flux, and section 3 presents the spatial distribution of the self-sputtered neutral flux. Finally, we discuss implications and conclude in section 4.

## 2. Self-Sputtered Fluxes

### 2.1. Exospheric Densities and Distributions

[4] While most suspected constituents of the lunar exosphere are to date unobserved [Stern, 1999; Cook *et al.*,

<sup>1</sup>Space Sciences Laboratory, University of California, Berkeley, California, USA.

<sup>2</sup>NASA Lunar Science Institute, Ames Research Center, Mountain View, California, USA.

<sup>3</sup>Goddard Planetary Heliophysics Institute, University of Maryland, Baltimore County, Baltimore, Maryland, USA.

<sup>4</sup>NASA Goddard Space Flight Center, Greenbelt, Maryland, USA.

Corresponding author: A. R. Poppe, Space Sciences Laboratory, University of California, 7 Gauss Way, Berkeley, CA 94720, USA. (poppe@ssl.berkeley.edu)

**Table 1.** The Mass, Photoionization Rate, and Subsolar Neutral Densities by Source Mechanism Used in This Modeling

| Species         | Mass (amu) | Photoionization Rate (s <sup>-1</sup> ) <sup>a</sup> | Subsolar Density (cm <sup>-3</sup> ) |               |               |                  |                 |
|-----------------|------------|--|--------------------------------------|---------------|---------------|------------------|-----------------|
|                 |            |  | PSD <sup>b</sup>                     | SW Sputtering | PS Sputtering | MIV <sup>c</sup> | Thermal         |
| He              | 4          | $5.25 \times 10^{-8}$                                | -                                    | -             | -             | -                | $2 \times 10^4$ |
| C               | 12         | $8.75 \times 10^{-7}$                                | -                                    | -             | -             | -                | $2 \times 10^2$ |
| O               | 16         | $4.57 \times 10^{-7}$                                | -                                    | 16.9          | 0.34          | 66.3             | -               |
| CH <sub>4</sub> | 16         | $5.9 \times 10^{-7}$                                 | -                                    | -             | -             | -                | $10^4$          |
| Na              | 23         | $1.6 \times 10^{-5}$                                 | 60                                   | 0.1           | 0.002         | 0.3              | -               |
| Mg              | 24.3       | $4.97 \times 10^{-7}$                                | -                                    | 2.3           | 0.046         | 5.5              | -               |
| Al              | 27         | $7 \times 10^{-4}$                                   | -                                    | 2.4           | 0.048         | 4.2              | -               |
| Si              | 28         | $4.43 \times 10^{-5}$                                | -                                    | 7.7           | 0.15          | 15.6             | -               |
| CO              | 28         | $6.95 \times 10^{-7}$                                | -                                    | -             | -             | -                | $2 \times 10^2$ |
| K               | 39         | $2 \times 10^{-5}$                                   | 19                                   | 0.03          | 0.0006        | 0.05             | -               |
| Ca              | 40         | $7.8 \times 10^{-5}$                                 | -                                    | 2.6           | 0.052         | 3.5              | -               |
| Ar              | 40         | $6.1 \times 10^{-7}$                                 | -                                    | -             | -             | -                | $5 \times 10^2$ |
| CO <sub>2</sub> | 44         | $1.22 \times 10^{-6}$                                | -                                    | -             | -             | -                | $2 \times 10^2$ |
| Ti              | 47         | $2.4 \times 10^{-6}$                                 | -                                    | 0.5           | 0.01          | 0.5              | -               |
| Fe              | 56         | $3.7 \times 10^{-6}$                                 | -                                    | 4.5           | 0.09          | 4.1              | -               |
| Xe              | 131        | $1.45 \times 10^{-8}$                                | -                                    | -             | -             | -                | $2 \times 10^3$ |

<sup>a</sup>Huebner *et al.* [1992].

<sup>b</sup>Photon-stimulated desorption.

<sup>c</sup>Micrometeoroid impact vaporization.

2013], recent advances in the understanding of relevant exospheric source and loss processes have allowed fairly comprehensive models of the exosphere to be constructed. For most of the regolith-derived elements (O, Mg, Al, Si, Ca, Ti, and Fe), we use the model of *Sarantos et al.* [2012b] which includes contributions from both micrometeoroid impact vaporization and charged-particle sputtering from the solar wind, which for these species, contribute roughly equal amounts to the density (the exception being Si and O, which have impact vaporization contributions roughly 2 and 4 times the charged-particle sputtering contribution, respectively). For plasma sheet sputtering, we scale the solar wind sputtered neutral densities down by a factor of 50 to accurately capture the decreased plasma flux in the plasma sheet. For Na and K, which are produced in the lunar exosphere predominantly through photon-stimulated desorption with a  $\cos^2 \alpha$  solar zenith angle distribution [*Yakshinskiy and Madey*, 1999], we take observational values for the density of approximately 60 and 19 cm<sup>-3</sup>, respectively [*Potter et al.*, 2000]. Noble gases Ar and Xe are modeled based on observations by Apollo-era instruments [*Hoffman et al.*, 1973; *Feldman and Morrison*, 1991] while recent measurements by the Lunar Reconnaissance Orbiter (LRO)/Lyman Alpha Mapping Project (LAMP) instrument are used for He [*Stern et al.*, 2012; *Feldman et al.*, 2012]. We note that direct measurements of He and Ar are solely on the lunar nightside due to the saturation of the Lunar Atmosphere Composition Experiment (LACE) instrument during lunar day and the orbital profile of the LRO spacecraft; however, theoretical arguments can predict the subsolar density of these species and we adopt these values for our modeling [*Hodges*, 1975]. We also note that the densities used for C, S, and Xe are upper limits [*Feldman and Morrison*, 1991]. Finally, we also include estimates for CH<sub>4</sub>, CO, and CO<sub>2</sub>, based on predawn LACE measurements [*Hodges*, 1975]; however, we note that these measurements are somewhat uncertain and subject to significant error. Table 1 lists the species, mass, photoionization rate (during solar minimum), and subsolar density

by source process for the exospheric constituents used in this model.

[5] In addition to assembling the neutral densities, we must also specify a spatial distribution for each species. We adopt a *Chamberlain* [1963]-type model with isotropic angular dependence which requires the specification of a neutral scale height, or equivalently, a neutral temperature,  $T_n$ . We note that a *Chamberlain* [1963]-type model may not be the most accurate choice for the more volatile elements in the lunar exosphere (i.e., CH<sub>4</sub>, CO, and CO<sub>2</sub>), yet in the absence of direct measurements of the spatial distribution of these species, we choose to employ the *Chamberlain* [1963]-type model and leave improvements to this assumption for future work. We use neutral temperatures of 385, 800, 1200, and 2000 K for thermal desorption, K photon-stimulated desorption, Na photon-stimulated desorption [*Yakshinskiy and Madey*, 1999], and micrometeoroid bombardment [*Sarantos et al.*, 2008], respectively. For charged-particle sputtering, previous work has shown that sputtered neutrals are best fit by a Sigmund-Thompson distribution [*Sigmund*, 1969], which for typical ion bombardment energies and binding energies of typical regolith species yields mean ejection energies of approximately 1 eV [*Wurz et al.*, 2007]. Therefore, we approximate the distribution of charged-particle sputtered neutrals with a 10,000 K Maxwellian distribution. Exospheric scale heights are then calculated using the neutral temperature for each source process and the relevant neutral masses. Scale heights range from 15 km for thermally accommodated Xe to 3200 km for sputtered O.

## 2.2. Plasma Environments

[6] As the Moon orbits the Earth, it encounters a range of ambient plasma environments. For purposes of calculating the self-sputtering flux, we broadly distinguish three environments:

[7] 1. The solar wind: Dominant throughout approximately 75% of the Moon's orbit around the Earth, the solar

wind consists of protons with a bulk energy of approximately 1 keV and magnetic field strengths ranging between 5 and 20 nT. The convection of the solar wind throughout the heliosphere generates a convection electric field at 1 AU with typical values ranging from approximately 1 to 10 mV/m. While the solar wind flow direction is fairly constant, the interplanetary magnetic field orientation is highly dynamic, resulting in a convection electric field that while always perpendicular to the flow is also variable in direction and magnitude. On the dayside lunar surface, the sum of the solar wind and photoemission currents typically drives the lunar surface a few volts positive in potential [Poppe and Horányi, 2010]. For the purposes of modeling the self-sputtering flux in the solar wind, the surface potential is negligible and only the energy gained from the solar wind convection electric field is considered. Nevertheless, the convection electric field is capable, depending on the species, of accelerating ions up to energies of 1–10 keV and higher [Halekas et al., 2012].

[8] 2. The terrestrial plasma sheet/plasma sheet boundary layer (PSBL): The Moon crosses the geomagnetic tail for approximately 25% of its orbit, where it periodically encounters the terrestrial plasma sheet and the plasma sheet boundary layer. The plasma sheet consists of a more tenuous yet hotter plasma than the solar wind, with proton densities between 0.1 and 1 cm<sup>-3</sup> and temperatures on the order of a keV, while the boundary layer is a transition region between the central plasma sheet and the tenuous tail lobes [Baumjohann et al., 1988, 1989]. In the plasma sheet, the magnetic field is often highly variable and turbulent; however, in the PSBL, the geomagnetic field remains predominantly aligned along the Sun-Earth (+X GSE) vector, similar to the tail lobes [Grigorenko et al., 2012]. The convection of the geomagnetic field lines from the tail lobes into the plasma sheet generates a convection electric field ranging from approximately 0.1 to 1 mV/m, roughly an order of magnitude less than that in the solar wind [Troshichev et al., 1999]. In the plasma sheet and the PSBL, the dayside lunar surface potential is often observed at several hundred volts negative with respect to the ambient environment [Halekas et al., 2005b, 2008], which recent particle-in-cell simulations have shown is due to nonmonotonic charging of the lunar surface [Poppe et al., 2011, 2012a]. The magnitude of this potential is mainly a function of the ambient electron temperature, with a small dependence on the ion temperature. The presence of this negative surface potential will accelerate incident pickup ions into the lunar surface and is a critical inclusion in our model.

[9] 3. The terrestrial tail lobes: The tail lobes are regions of relatively tenuous electron and ion densities ( $n \leq 0.1$  cm<sup>-3</sup>) formed as the Earth’s magnetic field is elongated anti-sunward under the pressure of the solar wind. In this environment, plasma sputtering of the lunar surface nearly completely ceases and the surface electrostatic potential increases dramatically to values ranging between +40 and +200 V [Reasoner and Burke, 1972; Harada et al., 2013]. Exospheric pickup ions have been observed in this environment [Tanaka et al., 2009; Poppe et al., 2012b]; however, analysis of both observations and modeling have concluded that the large electrostatic surface potential attained in the lobes reflects incident exospheric pickup ions before they are able to impact the lunar surface [Poppe et al., 2013].

Therefore, the self-sputtering process is highly suppressed in this environment, and we do not consider the tail lobes further in our calculations.

[10] For a range of both solar wind and plasma sheet/PSBL conditions, we modeled the exospheric pickup ion flux using a particle-tracing code. To limit the computational time required, we divided the list of ion species into several categories based on the ion mass and scale height (i.e., an ion mass of 24 amu and scale height of 400 km were used to represent micrometeoroid impact produced Na, Mg, Al, and Si, all of which have similar masses and scale heights). For each combination of ion mass, scale height, and ambient plasma conditions, we computed the trajectories of 500,000 ions, weighted each ion based on its starting position according to the Chamberlain [1963] spatial distribution, and recorded both the fraction of ions that impact the lunar surface (relative to those that escape the lunar environment) and the impacting differential ion energy flux. Figure 1 shows the differential energy flux distribution for five masses ( $m = 4, 16, 24, 40,$  and  $56$ ) with  $T_n = 2000$  K for one set of plasma conditions in both the plasma sheet/PSBL and the solar wind, respectively. Both figures also show the differential energy flux distribution for the ambient plasma (plasma sheet or solar wind, respectively) as a dashed line for comparison. Figure 1a shows that in the plasma sheet/PSBL, the combination of magnetotail convection and the surface potential can accelerate ions to energies up to and greater than 1 keV. For  $m = 4$  (He), the maximum energy attained is approximately 700 eV, which represents the maximum combination of energy obtained through convection ( $E_{\max} = 2m_i v_c^2$ , where  $m_i$  is the ion mass and  $v_c$  is the convection speed) and the energy obtained from the surface potential (500 eV in this case). For the heavier masses, ( $m = 16, 26, 40,$  and  $56$ ), the maximum energy obtained does not reach the maximum possible ( $E_m = 1335, 1850, 2590,$  and  $3400$  eV, respectively), but rather the maximum energy obtained by each mass decreases as a function of increasing mass. This trend is because as the ion mass increases, the scale height decreases (assuming a constant neutral temperature in this example) and ions are therefore born closer to the Moon and undergo less acceleration from the convection electric field before impacting the surface. Figure 1b shows a similar pattern for ions in the solar wind with two exceptions: the magnitude of the impact energy is roughly an order of magnitude higher due to the higher convection speed and electric field in the solar wind and mass 4 ions do not quite reach their theoretically maximum energy ( $E_{\max} \approx 17$  keV) as in the plasma sheet. Nevertheless, in both the plasma sheet and the solar wind, the combination of convection and surface electric fields accelerates ions up to keV and higher energies before they impact the lunar surface. Additionally, this modeling provides the total pickup ion flux by species to the lunar surface (in other words, the integral over energy of the differential energy flux) and while not shown here, is similar to that recently calculated by Sarantos et al. [2012a] providing an important check on our work.

### 2.3. Neutral Sputtering Yields

[11] Integral to the calculation of self-sputtering yields for any airless body is the neutral sputtering yield as a function of ion impact energy and mass. For our model, we use the TRIM.SP (Sputtering version of the Transport of Ions in

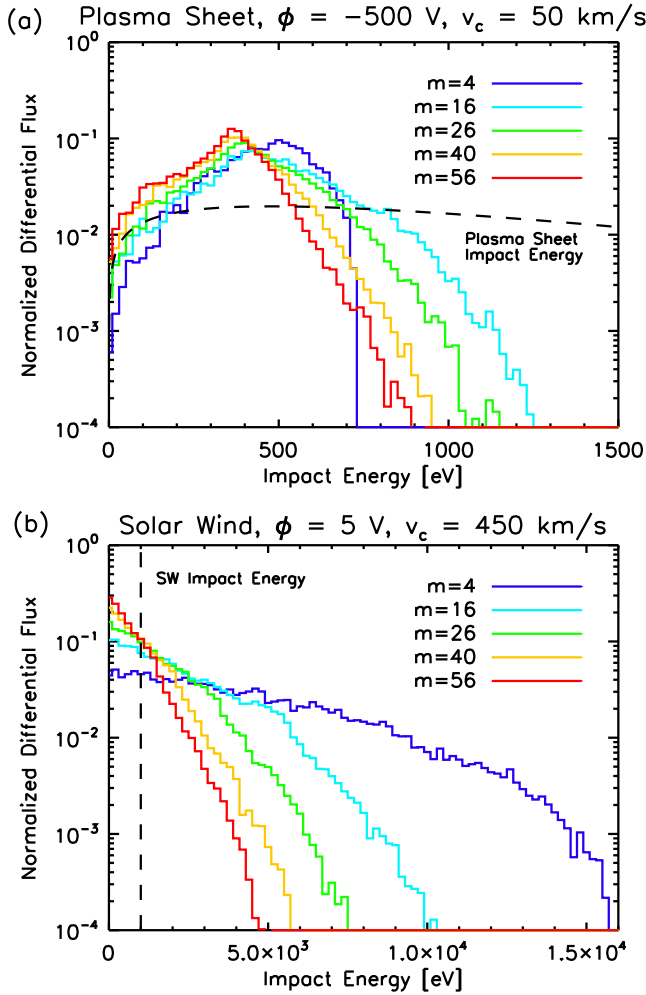


**Figure 1.** The differential flux of five different mass ions impacting the surface of the Moon under two different ambient plasma conditions: (a) in the terrestrial plasma sheet with a convection speed of 50 km/s and a surface potential of  $\phi = -500$  V, and (b) in the solar wind, with a convection speed of 450 km/s and a surface potential of  $\phi = 5$  V. Note the different x axis scales. The dashed lines in both panels indicates the impact energy of ambient protons.

Materials) results [Biersack and Haggmark, 1980; Biersack and Eckstein, 1984; Behrisch and Eckstein, 2007], specifically Figure 17 of Biersack and Eckstein [1984]. While these yields are specifically for a pure Ni target, experimental laboratory studies with  $\text{SiO}_2$  as a target have found equivalent neutral sputtering yields for heavy ion bombardment [Johnson and Baragiola, 1991]. The TRIM.SP results show that protons have a peak sputtering yield of approximately  $10^{-2}$  at an impact energy of roughly 1 keV with lower and higher energy cutoffs of approximately 100 eV and 10 keV, respectively. The overall magnitude of the yield increases steeply as a function of mass, from a peak yield of  $10^{-2}$  for 1 amu ( $\text{H}^+$ ) to a peak yield of approximately unity for 20 amu ( $\text{Ne}^+$ ). For masses larger than this, the increase in the yield magnitude slows with peak yields of  $\approx 5$  for 131 amu ( $\text{Xe}^+$ ). In addition to the increase in overall magnitude as a function of mass, the lower and upper cutoffs in energy also widen. The lower energy limit for an appreciable yield ( $\approx 10^{-3}$ )

decreases from 100 eV for protons to approximately 30–50 eV for the heaviest ions. Meanwhile, the upper energy cutoff increases from 10 keV for protons to values greater than 100 keV for heavier ions. The lower cutoff energies for higher impacting ion mass is especially important for our model, as it implies that even fairly low energy (30–100 eV) impacting heavy ions can sputter neutrals with yields far exceeding that for equivalent energy protons.

## 2.4. Total Self-Sputtered Flux

[12] The total neutral self-sputtered flux for a given set of plasma conditions is calculated by convolving the appropriate differential ion energy flux and the neutral sputtering yield as a function of impact energy and ion mass. Figure 2 shows the self-sputtered neutral flux from the lunar surface as a function of each incident exospheric species for (a) terrestrial plasma sheet conditions of  $v_c = 50$  km/s and  $\phi = -500$  V, and (b) solar wind conditions of  $B = 10$  nT and  $v_c = 450$  km/s, respectively. For the plasma sheet example, self-sputtered neutral fluxes from individual species range from approximately  $10^5$ – $10^6$   $\text{m}^{-2} \text{s}^{-1}$  ( $\text{Mg}^+$ ,  $\text{Ti}^+$ ) up to  $10^9$   $\text{m}^{-2} \text{s}^{-1}$  ( $\text{Al}^+$ ). The most efficient self-sputtering exospheric ions are  $\text{He}^+$ ,  $\text{Al}^+$ , and  $\text{CH}_4^+$  due to either high photoionization rates ( $\text{Al}^+$ ) or large surface densities ( $\text{He}^+$ ,  $\text{CH}_4^+$ ) and together produce approximately 75% of the self-sputtered neutral flux. Additional contributions come from  $\text{Na}^+$ ,  $\text{Si}^+$ , and  $\text{CO}^+$  (accounting for approximately 20% of the flux), while several species contribute negligibly ( $\text{C}^+$ ,  $\text{O}^+$ ,  $\text{Mg}^+$ ,  $\text{S}^+$ ,  $\text{K}^+$ ,  $\text{Ca}^+$ ,  $\text{Ar}^+$ ,  $\text{CO}_2^+$ ,  $\text{Ti}^+$ ,  $\text{Fe}^+$ , and  $\text{Xe}^+$ ). We note that  $\text{CO}^+$  and  $\text{CO}_2^+$  have ion production rates (density times photoionization rate) of the same magnitude as that of  $\text{Al}^+$ ,  $\text{Na}^+$ , and  $\text{Si}^+$ , for example, yet contribute relatively little to the self-sputtered flux. This difference is due to the scale height of each neutral species, which as discussed earlier, that controls the impact energy distribution for each species. As CO and  $\text{CO}_2$  are modeled as relatively cold, thermally accommodated species, they will have lower ion impact energies and in turn, lower self-sputtered fluxes than that from Al, Na, and Si, despite their relatively similar ion production rates.

[13] All together, the sum of the self-sputtering contributions in the plasma sheet from all incident exospheric species yields a net self-sputtered neutral flux of approximately  $2.5 \times 10^9$   $\text{m}^{-2} \text{s}^{-1}$ , averaged over the lunar dayside. In comparison, we can also estimate the neutral sputtered flux from the terrestrial plasma sheet assuming a total ion density of  $0.5 \text{ cm}^{-3}$  with 5%  $\text{He}^+$  contribution [Christon et al., 1989]. We find a plasma sheet sputtered flux at the subsolar point of  $\Gamma_{\text{ps},o} = 2 \times 10^9$   $\text{m}^{-2} \text{s}^{-1}$ , and assuming a  $\cos \alpha$  solar zenith angle dependence, derive a dayside-average sputtered flux of  $(\Gamma_{\text{ps}}) = (4/\pi^2)\Gamma_{\text{ps},o} = 8.1 \times 10^8$   $\text{m}^{-2} \text{s}^{-1}$ . The total self-sputtered and total plasma sheet sputtered neutral fluxes are compared in Figure 2 as dashed black and red lines, respectively, showing that for these plasma parameters, the self-sputtered flux (summed over all outgoing neutral species) is approximately 5 times the plasma sheet sputtered flux. Indeed, sputtering induced by exospheric  $\text{Al}^+$  ions equals the mean plasma sheet sputtered flux. We do note that variations in the plasma sheet density, temperature, and composition will cause the plasma sheet sputtered flux to vary over approximately an order of magnitude above and below the quoted value.

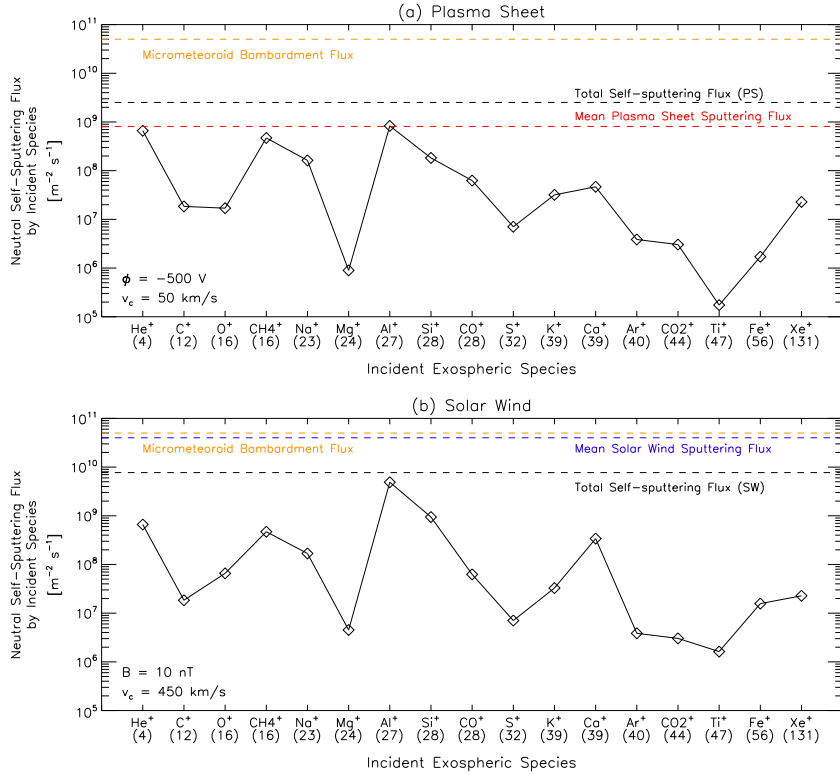


**Figure 2.** The globally averaged neutral self-sputtered flux in the (a) plasma sheet/PSBL and (b) the solar wind as a function of the incident heavy exospheric species. The dashed black line shows the total self-sputtered flux in each case while the dashed red line shows the mean plasma sheet neutral sputtered flux, the orange line denotes the estimated micrometeoroid bombardment produced flux, and the blue line denotes the solar wind sputtered flux.

[14] In Figure 2b, the self-sputtered flux by species in the solar wind shows an increase in the self-sputtered flux from solar wind sputtered neutrals (O, Mg, Al, Si, Ca, Ti, and Fe), reflecting the much higher plasma flux and neutral density of the exosphere in the solar wind. The total self-sputtered flux in the solar wind, summed over all incident species, is approximately  $8 \times 10^9 \text{ m}^{-2} \text{ s}^{-1}$ . This is roughly 20% of the dayside-averaged solar wind sputtered flux of  $4 \times 10^{10} \text{ m}^{-2} \text{ s}^{-1}$  or the micrometeoroid bombardment flux of  $5 \times 10^{10} \text{ m}^{-2} \text{ s}^{-1}$ , implying that self-sputtering is an important, yet not dominant, contributor to the lunar exosphere.

[15] We repeated the calculation of the total self-sputtered flux in the lunar exosphere over ranges of the ambient plasma parameters in both the solar wind and the plasma sheet. For the solar wind, we varied the strength of the convection electric field from that found for a relatively slow solar wind with weak magnetic field ( $v_{\text{sw}} = 250 \text{ km/s}$ ,  $B = 5 \text{ nT}$ ,  $E_c = 1.25 \text{ mV/m}$ ) to that for fast solar wind speed with a strong magnetic field ( $v_{\text{sw}} = 650 \text{ km/s}$ ,  $B = 20 \text{ nT}$ ,  $E_c = 12.5 \text{ mV/m}$ ), spanning approximately 1 order of magnitude in convection electric field strength. Figure 3a shows the total self-sputtered flux as a function of the solar wind convection electric field, compared alongside estimates for the dayside-averaged solar wind sputtered flux and the micrometeoroid bombardment vaporization flux [Morgan and Killen, 1997; Sarantos et al., 2012b]. For the solar wind sputtered flux, we included sputtering from solar wind

helium, which can add approximately 10–20% to the total sputtered flux, depending on the relative concentration of alpha particles in the solar wind. Thus, in the solar wind, the spatially averaged self-sputtered flux is roughly 2 to 5 times less than the solar wind sputtered or micrometeoroid bombardment neutral flux.

[16] For the plasma sheet, we varied both the surface potential from  $-10 \text{ V}$  to  $-500 \text{ V}$  and the convection speed from  $10 \text{ km/s}$  (dotted line) to  $50 \text{ km/s}$  (solid line) and showed the results in Figure 3b. Generally, as the magnitude of the surface potential and the convection speed increases, the self-sputtered flux also increases mainly due to higher ion impact energies and higher corresponding neutral sputtering yields. At low surface potentials ( $\phi = -10 \text{ V}$ ), the convection speed plays a significant role in the self-sputtered flux, while for high surface potentials ( $\phi = -500 \text{ V}$ ), the self-sputtered flux is nearly identical across convection speeds. The self-sputtered flux in the plasma sheet generally ranges from 1 order of magnitude less than up to approximately 5 times the dayside-averaged plasma sheet sputtered flux. At its greatest, the dayside-averaged self-sputtered flux is approximately 10% of the micrometeoroid bombardment neutral production flux, although we note that anisotropies in the pickup ion flux (discussed in the next section) imply that specific regions of the lunar dayside may be self-sputtered locally at fluxes comparable to micrometeoroid bombardment vaporization.

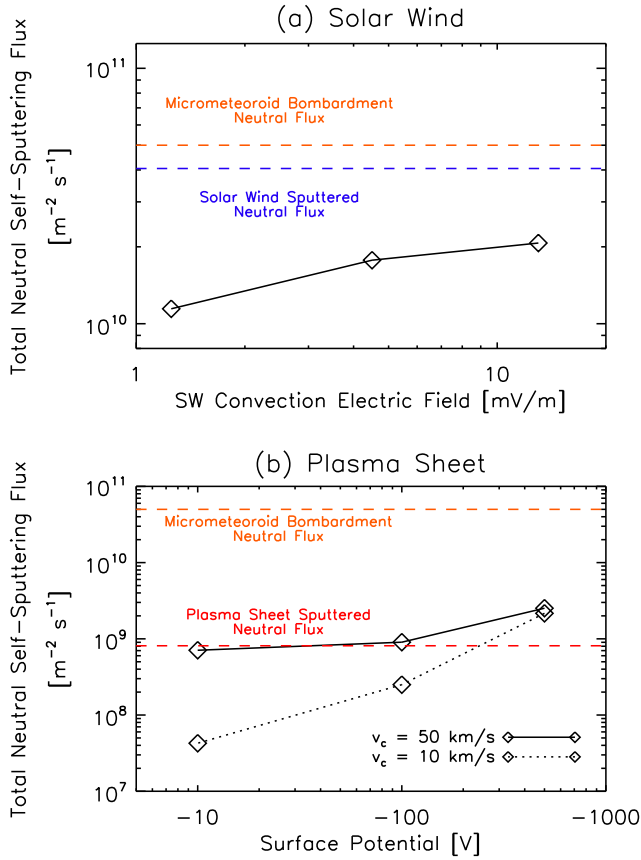


**Figure 3.** The total sputtered neutral flux (a) in the solar wind, as a function of the solar wind convection electric field, and (b) in the plasma sheet, as a function of the negative electrostatic surface potential for two convection velocities. Red and blue lines denote the globally averaged solar wind and plasma sheet sputtered neutral flux, respectively, while the orange line denotes the globally averaged micrometeoroid bombardment neutral flux.

### 3. Spatial Distribution

[17] In addition to calculating globally averaged self-sputtered fluxes, our model can be used to investigate the spatial dependence of the self-sputtering process. To first order, the exospheric pickup ion flux should “illuminate” one hemisphere of the lunar surface governed by the direction of the convection electric field; however, several effects may modify this simple picture including finite ion gyroradii, the electrostatic surface potential, and anisotropies in the existing exospheric neutral population. While our model does not consider the latter-most effect, we can explore the role of the former two effects. When calculating the ion impact energies shown in Figure 1, our model also tracks the impact location of the exospheric ion. By weighting the impact location frequency by the chosen exospheric distribution and dividing by the appropriate surface area, the local self-sputtered neutral flux as a function of lunar longitude and latitude, as well as the impacting ion species, can be calculated. Figure 3 shows the spatial distribution of the self-sputtered neutral flux for two impacting ion species,  $m = 4$  and  $m = 24$ , for two ambient plasma conditions, solar wind ( $v_c = 450 \text{ km/s}$ ,  $B = 10 \text{ nT}$ ) and plasma sheet ( $v_c = 50 \text{ km/s}$ ,  $\phi = -500 \text{ V}$ ),

respectively, relative to the globally averaged flux. Additionally, the convection coordinate system ( $B$ ,  $v_c$ ,  $E_c$ ) is depicted in the lower left-hand corner of each panel for reference.

[18] In the solar wind (Figures 3a and 3b), we orient the convection coordinate system such that the solar wind velocity is into the page and the magnetic field is horizontal (i.e., in the ecliptic plane), which dictates that the convection electric field points toward ecliptic north. Under these conditions, newly born ions will be accelerated northward along the convection electric field before gyrating around the interplanetary magnetic field and should illuminate the southern lunar hemisphere. To first order, Figures 4a and 4b confirm this, although the self-sputtered neutral flux induced by  $m = 4$  ions extends into the northern lunar hemisphere while self-sputtering from the heavier  $m = 24$  ions does not. This feature is due to the smaller ion gyroradius (approximately  $1800 \text{ km}$ ) for  $m = 4$  ions relative to that for  $m = 24$  or any heavier ions. As lighter ions are produced and picked up by the solar wind convection, their smaller gyroradius implies significant curvature in the ion trajectory allowing a fraction of the lighter ions to gyrate into and impact the northern lunar hemisphere. In contrast, Figure 4b shows a very sharp drop in self-sputtered neutral fluxes along the lunar equator for heavier masses as the larger gyroradius prevents ion access to the northern hemisphere. Noteworthy in both cases is the local enhancement (up to an order of magnitude) of self-sputtered neutral fluxes at the point “illuminated” by the convection electric field (in this case, the lunar southern pole) relative to the globally averaged flux.

[19] In contrast to the solar wind case, Figures 4c and 4d show the spatial distribution of self-sputtered fluxes in the plasma sheet for  $m = 4$  and  $24$  ions, respectively. The coordinate system for this environment has the magnetic field out of the page, the convection velocity horizontal (in the ecliptic plane) and the convection electric field northward. Both ion masses show maxima in the self-sputtered flux over the southern lunar pole similar to the solar wind case; however, the self-sputtered flux extends at significant levels far into the northern hemisphere. This effect is largely attributable to the order of magnitude decrease in the gyroradius of all ions since the convection speed in the magnetotail ( $50 \text{ km/s}$  in this case) is roughly an order of magnitude less than in the solar wind. Additionally, the presence of the large surface potential in the plasma sheet ( $\phi = -500 \text{ V}$  in this case) over the entire lunar dayside also contributes broadly to the self-sputtering flux by accelerating ions born from the very bottom of the exospheric scale height into the lunar surface regardless of longitude or latitude.

[20] Importantly, in both the solar wind and in the plasma sheet, the spatial distributions of self-sputtered neutral fluxes are highly anisotropic and dependent on the ambient plasma parameters. While we have shown one convection geometry in both the solar wind and in the plasma sheet, the time variation of plasma conditions is important to consider. In the solar wind, the flow velocity remains fairly steady in direction while the interplanetary magnetic field is quite variable, implying that at any given time, the self-sputtering flux is “illuminating” a different hemisphere of the Moon. While we have shown spatial distributions of the self-sputtered flux for the interplanetary magnetic field (IMF) in the ecliptic plane, other IMF geometries do exist in the solar wind. When the IMF has a dominant  $B_z$  component,

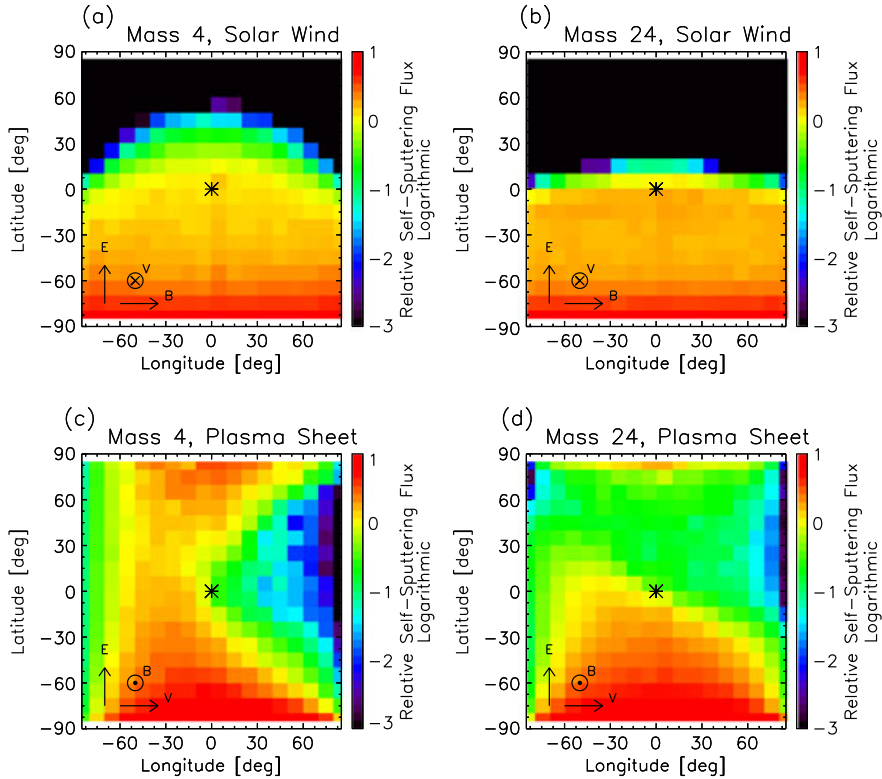


**Figure 4.** The spatial distribution of self-sputtered neutral fluxes from the lunar surface for two masses ( $m = 4, 24$ ) under two conditions (solar wind and plasma sheet) on the lunar dayside as a function of lunar longitude and latitude. The asterisk in each panel marks the subsolar point. Additionally, the convection coordinate system ( $B, v, E = -v \times B$ ) is shown in the lower left corner of each panel.

for example, the pickup ions will gyrate in planes parallel to the ecliptic and will impact the dawnward or duskward limb (depending on the sign of  $B_z$ ), rather than the polar regions. Also, for cases where the IMF is parallel to the solar wind flow  $\mathbf{B} = \langle B_x, 0, 0 \rangle$ , the convection electric field will drop to zero as will the self-sputtering flux. Statistically, the interplanetary magnetic field is preferentially in the ecliptic plane with the convection electric field being predominantly ecliptic north/south [Luhmann *et al.*, 1993] implying that averaged over long periods of time in the solar wind, the self-sputtering flux mainly affects the lunar polar regions, rather than the equatorial regions. Convection in the magnetotail can be quite variable, especially at lunar distances down tail; however, periods of steady magnetospheric convection (SMC) have been documented lasting up to 12 h [Sergeev *et al.*, 1996; O’Brien *et al.*, 2002], which implies that exospheric species whose photoionization lifetimes are shorter than the typical SMC events will respond quickly to the steady convection.  $\text{Al}^+$  has the shortest photoionization lifetime ( $\approx 25$  min) of the species we consider and due to this is also the dominant self-sputtering exospheric ion. With such a short photoionization lifetime, the self-sputtered flux will respond quickly to extended SMC events and may be able to temporarily build distinct asymmetries in the self-sputtered neutral exospheric component while and slightly after the Moon is exposed to the plasma sheet/PSBL.

[21] Given the anisotropies in the self-sputtered flux across the lunar dayside, we can explore whether self-sputtering will locally exceed solar wind or plasma sheet

sputtering. To calculate this, we summed over the individual spatially resolved self-sputtering contributions (i.e., Figure 4) from each exospheric pickup ion species to calculate the total spatially resolved self-sputtered flux. The solar wind and plasma sheet sputtering fluxes were modeled as  $\cos \alpha$  solar zenith angle dependent, centered at the subsolar point. We took the ratio of the self-sputtered flux in the appropriate plasma environment and divided by either the solar wind and plasma sheet sputtering flux, shown in Figures 5a and 5b, respectively. For both cases, we used the same convection coordinate system as presented in Figure 4 with the convection electric field oriented northward. In the solar wind, solar wind sputtering dominates completely in the northern hemisphere as expected since very little exospheric pickup ion flux reaches the northern lunar hemisphere. Solar wind sputtering also dominates over self-sputtering across most of the southern hemisphere; although toward the southern pole and the lower latitude terminator region, the ratio reaches unity (denoted by the solid line). Southward of this, the local self-sputtered flux exceeds the local solar wind sputtering flux by more than an order of magnitude. Figure 5b shows that the ratio of plasma sheet sputtering to self-sputtering is spatially more complex. While plasma sheet sputtering exceeds self-sputtering by 1 to 2 orders of magnitude roughly over the northern, duskward quadrant, self-sputtering dominates over much over the southern hemisphere, the dawnward quadrant, and even at the northern lunar pole. Also, at its extreme, the self-sputtering to plasma sheet sputtering ratio exceeds 2

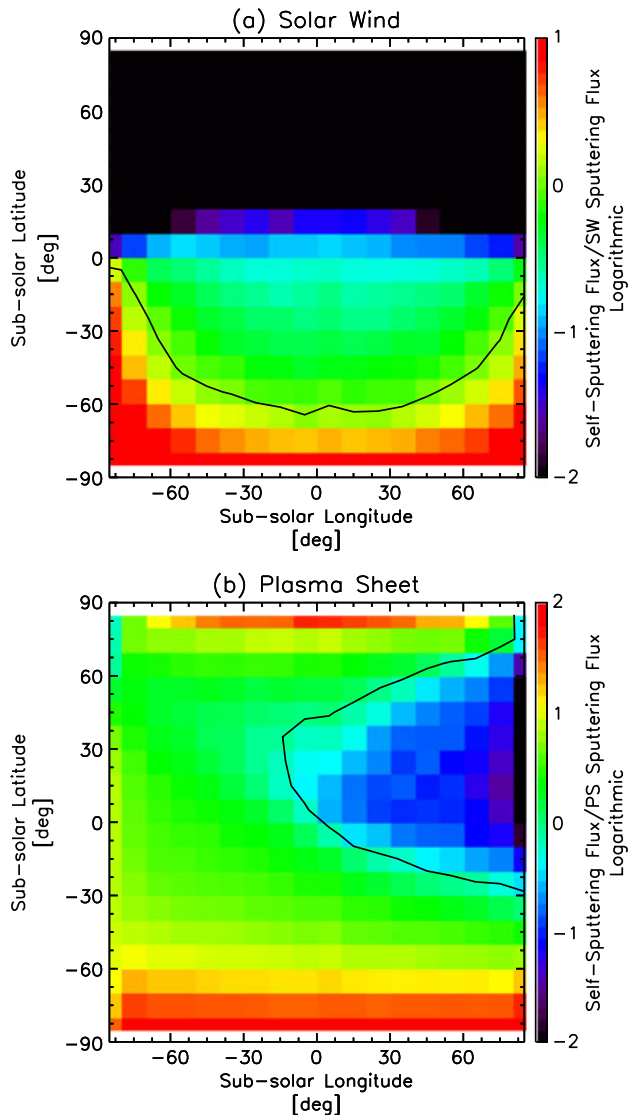


**Figure 5.** (a) The ratio of the self-sputtered neutral flux (summed over all incident exospheric pickup ion species) in the solar wind to the solar wind sputtered flux as a function of lunar longitude and latitude on the dayside. (b) The same as Figure 5a but for the plasma sheet. The solid contour in both panels marks the ratio value of unity for reference. Note the change in color scale between panels.

orders of magnitude at the southern lunar pole (note the slightly different color scales between Figures 5a and 5b). Thus, while in an average sense, the self-sputtered flux is less than solar wind sputtering and roughly equal to plasma sheet sputtering, the highly anisotropic nature of the self-sputtering process leads to regions of the lunar surface where self-sputtering becomes the dominant charged-particle sputtering process. While not shown here, we can also compare the spatially resolved self-sputtering flux to the neutral flux from micrometeoroid bombardment, which, if assumed to be isotropic generates a neutral flux of approximately  $5 \times 10^{10} \text{ m}^{-2} \text{ s}^{-1}$  [Morgan and Killen, 1997; Sarantos et al., 2012b]. In comparison, the maximum local self-sputtered fluxes for typical solar wind and plasma sheet cases are  $1.8 \times 10^{11}$  and  $1.2 \times 10^{11} \text{ m}^{-2} \text{ s}^{-1}$ , respectively. Thus, at

its greatest location, self-sputtering produces a local neutral flux up to almost 4 times that from micrometeoroid bombardment.

#### 4. Discussion and Conclusion

[22] The calculations presented here have shown that exospheric self-sputtering may play an important role in maintaining the tenuous lunar neutral exosphere. Many processes contribute to the generation of the lunar exosphere and spatially averaged over the lunar dayside, micrometeoroid bombardment and solar wind charged-particle sputtering are dominant, while plasma sheet sputtering (when the Moon is in the magnetotail) and self-sputtering are roughly an order of magnitude less. For Na and K specifically, photon-stimulated desorption exceeds all other generation mechanisms [Potter and Morgan, 1998; Sarantos et al., 2012b]. Our modeling does indicate, however, that owing to the anisotropic nature of the exospheric pickup ion flux and its resulting sputtering distribution on the lunar dayside, local self-sputtered neutral fluxes may equal or exceed fluxes from charged-particle sputtering (both in the solar wind and the plasma sheet) and micrometeoroid bombardment. We expect this to be highly variable in time, especially in the solar wind, where the interplanetary magnetic field undergoes rapid changes on timescales of seconds to minutes.

[23] Knowledge of the ambient plasma and electromagnetic environment is critical for calculating the self-sputtered flux. In the solar wind, the controlling electromagnetic parameter is the strength of the convection electric field, as the lunar surface potential is negligible compared to typical pickup ion energies [Poppe and Horányi, 2010]. In contrast, self-sputtering in the terrestrial magnetotail is governed by both the convection electric field and the lunar surface potential. The convection electric field is typically an order of magnitude less than in the solar wind [Troshichev et al., 1999], while the lunar surface potential reaches magnitudes much greater than or less than in the solar wind, depending on the ambient plasma environment. In the tail lobes, observational evidence has suggested that the surface potential exceeds +40 V and can reach values as high as +200 V [Reasoner and Burke, 1972; Harada et al., 2013], while in the plasma sheet or PSBL, observations have shown that negative, nonmonotonic electrostatic potentials can exceed -500 V [Halekas et al., 2008; Poppe et al., 2011, 2012a]. The combination of relatively weak convection electric fields and enhanced lunar surface potentials implies that the surface potential becomes the controlling electromagnetic parameter, with self-sputtering nearly absent in the tail lobes as the surface potential either reflects the incident pickup ions [Poppe et al., 2012b; Harada et al., 2013] or decelerates ions to such a degree that the neutral sputtering yield is negligible. In the plasma sheet and PSBL, the opposite occurs, where the lunar surface potential enhances both the flux and the impact energy of lunar pickup ions, resulting in a relatively high self-sputtered neutral flux. At other airless bodies, electrostatic surface potentials may play an important role in either promoting or inhibiting neutral self-sputtering fluxes and should be investigated [Ip, 1996; Ip et al., 1998; Roussos et al., 2010].

[24] Recently reported density limits from the Lunar Reconnaissance Orbiter LAMP instrument on numerous

species thought to be in the lunar exosphere [Cook *et al.*, 2013] may influence the results presented here, although we do not at this time include these limits mainly because we are unsure how to propagate density limits made on the lunar nightside at approximately 10 P.M. and 4 A.M. local time to putative densities at the lunar subsolar point (local noon). Given the unconstrained angular distributions of most lunar exospheric species, local densities could exist on the lunar dayside higher than the limits established by LRO/LAMP, especially for those species generated by solar wind charged-particle sputtering [Wurz *et al.*, 2007; Sarantos *et al.*, 2012b]. Nevertheless, we did repeat our analysis implementing the LRO/LAMP limits assuming that the limits constrain only the exospheric contribution from micrometeoroid bombardment, which is expected to be roughly isotropic. We converted the LRO/LAMP limits for  $T_n = 120$  K to  $T_n = 2000$  K to appropriately account for the expected temperature of the micrometeoroid bombardment component which decreased the upper limits by a factor of approximately 20 (J. Cook, personal communication, 2013). We used these upper limits for the micrometeoroid bombardment component of the exosphere, but left the solar wind and plasma sheet sputtering densities the same as that calculated in Sarantos *et al.* [2012b]. Under this condition, the self-sputtered flux dropped by approximately 10% in the solar wind and 50% in the plasma sheet, respectively, mainly due to a decrease in the  $\text{Al}^+$  neutral density and the corresponding  $\text{Al}^+$ -induced self-sputtered neutral flux. Nevertheless, self-sputtering by the solar wind or plasma sheet sputtered exospheric component still contributes a significant portion of the self-sputtered flux, regardless of the LRO/LAMP constraints.

[25] An important implication of this work is the self-sputtered flux that may arise inside craters or other topographical features that are shielded from direct access from the solar wind. Recent kinetic plasma simulations have shown that as the solar wind convects past permanently shadowed craters, relatively strong ambipolar electric fields develop pointing into the crater thus accelerating ions into the shadowed regions to balance the greater solar wind electron flux [Zimmerman *et al.*, 2011, 2012]. In these simulations, it was found that surfaces within shadowed craters can attain electrostatic potentials hundreds of volts more negative than the ambient solar wind under both typical and solar storm conditions. Therefore, any exospheric pickup ion that entered lunar polar craters would be accelerated through several hundred volts (in addition to the potential drop already experienced from the convection electric field) before impacting the crater floor. Calculations of the solar wind proton flux to shadowed crater floors due to the ambipolar electrostatic field for typical solar wind conditions range from approximately  $10^8$  to  $10^{10}$   $\text{m}^{-2} \text{s}^{-1}$  [Zimmerman *et al.*, 2012, Figure 3]. With a proton sputtering yield of 0.01 [Biersack and Eckstein, 1984; Behrisch and Eckstein, 2007], this provides a neutral sputtered flux of approximately  $10^6$  to  $10^8$   $\text{m}^{-2} \text{s}^{-1}$ . In comparison, the neutral self-sputtered flux from incident heavy exospheric ions at the lunar poles can exceed approximately  $10^{11}$   $\text{m}^{-2} \text{s}^{-1}$  during times when the solar wind convection electric field is oriented in the north/south direction. Thus, while solar wind entry into shadowed craters may drive the overall formation of the electrostatic environment within such a crater, the

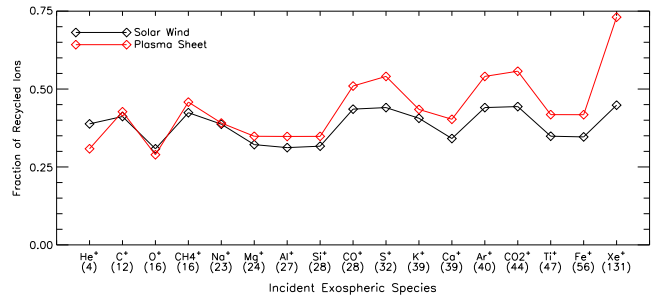


**Figure 6.** The fraction of recycled ions by species for typical conditions in the solar wind (black) and the plasma sheet (red).

flux of heavy exospheric pickup ions may outstrip the solar wind protons as the dominant sputtering agent of shadowed crater floors. Such a sputtering source should be considered when addressing the source and loss processes governing the potential sequestration of volatiles within shadowed craters [Crider and Vondrak, 2003a, 2003b; Colaprete *et al.*, 2010; Gladstone *et al.*, 2010]. Alternatively, the flux of pickup ions into permanently shadowed regions on the Moon may represent an efficient channel to implant a host of exospheric species into the permanently shadowed lunar regolith, such as were observed during the Lunar Crater Observation and Sensing Satellite impact [Gladstone *et al.*, 2010; Schultz *et al.*, 2010].

[26] We also note that species with large-scale heights and relatively small gyroradii (compared to a lunar radius) may be able to effectively access the lunar nightside and sputter neutrals that are thermally adsorbed to the cold nightside surface. The most likely specie to accomplish this is  $\text{He}^+$  which is known to have a large-scale height and has been measured near the lunar terminator [Hodges, 1975; Stern *et al.*, 2012; Feldman *et al.*, 2012]; although in the plasma sheet/PSBL, a wider range of heavier species with smaller gyroradii (given the lower convection speed) may also be able to access the lunar nightside. In the solar wind, the ionized products of such species would not only be accelerated by the convection electric field but also would experience additional acceleration through the ambipolar electric field generated around the lunar wake [Halekas *et al.*, 2005a; Farrell *et al.*, 2007], ensuring relatively high energy impacts and an appreciable neutral sputtering yield [Biersack and Eckstein, 1984]. The strength and distribution of the ambipolar electric field is a function of the ambient solar wind parameters and is expected to vary along with solar wind plasma parameters. While we have not addressed such an effect here, the inclusion of an ambipolar electric field in the self-sputtering model is suggested as future work in an effort to assess the robustness of lunar nightside cold trapping on various condensable species [Hodges *et al.*, 1973; Hodges, 1980; Killen, 2002].

[27] The self-sputtering model presented here can also be used to calculate the fraction of exospheric ions that are recycled back to the lunar surface, rather than escaping into either interplanetary space or the terrestrial magnetotail. Pickup ion recycling has important implications for the equilibrium of exospheric species both in the exosphere and in the surface itself and has been extensively studied at Mercury [Leblanc *et al.*, 2003; Killen *et al.*, 2004] and

proposed at Europa [Ip et al., 1998; Cipriani et al., 2008]. In Figure 6, we show the fraction of recycled exospheric pickup ions as a function of species for typical solar wind and plasma sheet conditions, respectively. Recycling fractions range from as low as 25% ( $O^+$ , plasma sheet) up to 75% ( $Xe^+$ , plasma sheet), with a general increase in recycling as a function of mass. This increase is mainly driven by the decreasing scale height as a function of mass which causes the Moon to represent a relatively larger obstacle to the escaping pickup ion outflow. Notably, the escape fraction for the thermally modeled species ( $C^+$ ,  $CH_4^+$ ,  $CO^+$ ,  $S^+$ ,  $Ar^+$ ,  $CO_2^+$ , and  $Xe^+$ ) typically shows increases over their hotter counterparts, again due to their smaller scale heights. In the plasma sheet, the increase is enhanced for the thermal species because the negative electrostatic potential above the lunar surface traps pickup ions originating in the lowest portion of the exosphere, where the neutral density is highest. Given the asymmetries in the exospheric pickup ion flux to the lunar surface discussed in section 3, we also suggest that extended periods of steady convection could implant ions asymmetrically enough to affect later thermal desorption yields. While such steady convection is not likely in the solar wind, steady magnetotail convection could last long enough to produce noticeable shifts in thermally desorbed species [Sergeev et al., 1996; O'Brien et al., 2002]. Such an effect would be most prominent for species whose photoionization lifetimes were shorter than the length of the steady convection (i.e.,  $Al^+$ , which has a photoionization lifetime of approximately 25 min).

[28] The self-sputtering flux at the Moon may also be greatly enhanced during the passage of a coronal mass ejection (CME). A recent collaborative study investigating the response of the coupled plasma and neutral environment at the Moon due to a CME passage found that the lunar exosphere can temporarily gain a significant amount of mass (between 10 and 50 times normal) for approximately 1–2 days following the CME passage due to the enhanced solar wind sputtering rates [Farrell et al., 2012; Killen et al., 2012]. During this period of enhanced exospheric densities, the pickup ion flux to the lunar surface and the corresponding self-sputtered neutral flux should be both greatly enhanced. While the Killen et al. [2012] model predicted that the exosphere should relax back to its typical solar wind-driven state within 10–50 h, the presence of an enhanced self-sputtered flux in the exosphere may act to prolong the enhanced exospheric state. A time-dependent exospheric Monte Carlo model of the exosphere with the inclusion of a self-sputtering production term is suggested as a future investigation.

[29] The calculations presented here will be of use in interpreting in situ and remote sensing observations of the lunar exosphere by the upcoming Lunar Atmosphere and Dust Environment Explorer (LADEE), slated to launch in fall 2013 [Delory et al., 2009]. Observations by LADEE will constrain both the neutral densities and spatial distributions of many suspected lunar exospheric species, which will in turn allow for constraints on the various source processes that generate the lunar exosphere. Appropriately accounting for the self-sputtered neutral component may be critical in fully understanding and interpreting the LADEE observations and the lunar exosphere as a whole. Additionally, observations by the Acceleration, Reconnection,

Turbulence, and Electrodynamics of the Moon's Interaction with the Sun mission [Angelopoulos, 2011; Sibeck et al., 2011] of pickup ion fluxes at the Moon may provide additional information linking heavy exospheric pickup ion fluxes to the generation of exospheric neutrals when combined with LADEE observations.

[30] **Acknowledgments.** The authors gratefully acknowledge support from the NASA Lunar Science Institute and NASA's Lunar Advanced Science and Exploration Research program, grants NNX13AJ97G (A.R.P. and J.S.H.) and NNX11AQ65G (M.S.). The authors are grateful to J. Cook and S. A. Stern at the Southwest Research Institute for assistance in the interpretation of LRO/LAMP exospheric results. A.R.P. and J.S.H. also acknowledge the International Space Science Institute for hosting a workshop from which this work benefited.

## References

- Angelopoulos, V. (2011), The ARTEMIS mission, *Space Sci. Rev.*, 165, 3–25.
- Baumjohann, W., G. Paschmann, N. Sckopke, C. A. Cattell, and C. W. Carlson (1988), Average ion moments in the plasma sheet boundary layer, *J. Geophys. Res.*, 93(A10), 11,507–11,520.
- Baumjohann, W., G. Paschmann, and C. A. Cattell (1989), Average plasma properties in the central plasma sheet, *J. Geophys. Res.*, 94(A6), 6597–6606.
- Behrisch, R., and W. Eckstein (2007), *Sputtering by Particle Bombardment: Experiments and Computer Calculations From Threshold to MeV Energies*, vol. 110, Springer, Berlin and Heidelberg, Germany.
- Biersack, J. P., and W. Eckstein (1984), Sputtering studies with the Monte Carlo program TRIM.SP, *Appl. Phys. A*, 34, 73–94.
- Biersack, J. P., and L. G. Haggmark (1980), A Monte Carlo computer program for the transport of energetic ions in amorphous targets, *Nuc. Instr. Meth.*, 174(1-2), 257–269.
- Chamberlain, J. W. (1963), Planetary coronae and atmospheric evaporation, *Planet. Space Sci.*, 11, 901–960.
- Christon, S. P., D. J. Williams, and D. G. Mitchell (1989), Spectral characteristics of plasma sheet ion and electron populations during undisturbed geomagnetic conditions, *J. Geophys. Res.*, 94(A10), 13,409–13,424.
- Cipriani, F., F. Leblanc, O. Witasse, and R. E. Johnson (2008), Sodium recycling at Europa: What do we learn from the sodium cloud variability, *Geophys. Res. Lett.*, 35, L19201, doi:10.1029/2008GL035061.
- Colaprete, A., et al. (2010), Detection of water in the LCROSS ejecta plume, *Science*, 330, 463–468.
- Cook, J. C., S. A. Stern, P. D. Feldman, G. R. Gladstone, K. D. Retherford, and C. C. C. Tsang (2013), New upper limits on numerous atmospheric species in the native lunar atmosphere, *Icarus*, 225, 681–687.
- Crider, D. H., and R. R. Vondrak (2003a), Space weathering effects on lunar cold trap deposits, *J. Geophys. Res.*, 108(E7), 5079, doi:10.1029/2002JE002030.
- Crider, D. H., and R. R. Vondrak (2003b), Space weathering of ice layers in lunar cold traps, *Adv. Space Res.*, 31(11), 2293–2298.
- Delory, G. T., R. Elphic, T. Morgan, A. Colaprete, M. Horányi, P. Mahaffy, B. Hine, and D. Boroson (2009), The Lunar Atmosphere and Dust Environment Explorer (LADEE), in *Lunar and Planetary Science Conference Proceedings XL*, vol. 40, Lunar and Planetary Science Institute, The Woodlands, TX.
- Farrell, W. M., T. J. Stubbs, R. R. Vondrak, G. T. Delory, and J. S. Halekas (2007), Complex electric fields near the lunar terminator: The near-surface wake and accelerated dust, *Geophys. Res. Lett.*, 34, L14201, doi:10.1029/2007GL029312.
- Farrell, W. M., et al. (2012), Solar-Storm/Lunar Atmosphere Model (SSLAM): An overview of the effort and description of the driving storm environment, *J. Geophys. Res.*, 117, E00K04, doi:10.1029/2012JE004070.
- Feldman, P. D., and D. Morrison (1991), The Apollo 17 ultraviolet spectrometer: Lunar atmosphere measurements revisited, *Geophys. Res. Lett.*, 18(11), 2105–2109.
- Feldman, P. D., et al. (2012), Temporal variability of lunar exospheric helium during January 2012 from LRO/LAMP, *Icarus*, 221, 854–858.
- Gladstone, G. R., et al. (2010), LRO-LAMP observations of the LCROSS impact plume, *Science*, 330, 472–476.
- Grigorenko, E. E., R. Koleva, and J.-A. Sauvaud (2012), On the problem of plasma sheet boundary layer identification from plasma moments in Earth's magnetotail, *Ann. Geophys.*, 30, 1331–1343.
- Halekas, J. S., S. D. Bale, D. L. Mitchell, and R. P. Lin (2005a), Electrons and magnetic fields in the lunar plasma wake, *J. Geophys. Res.*, 110, A07222, doi:10.1029/2004JA010991.

- Halekas, J. S., R. P. Lin, and D. L. Mitchell (2005b), Large negative lunar surface potentials in sunlight and shadow, *Geophys. Res. Lett.*, *32*, L09102, doi:10.1029/2005GL022627.
- Halekas, J. S., G. T. Delory, R. P. Lin, T. J. Stubbs, and W. M. Farrell (2008), Lunar prospector observations of the electrostatic potential of the lunar surface and its response to incident currents, *J. Geophys. Res.*, *113*(A09102), doi:10.1029/2008JA013194.
- Halekas, J. S., A. R. Poppe, G. T. Delory, M. Sarantos, W. M. Farrell, V. Angelopoulos, and J. P. McFadden (2012), Lunar pickup ions observed by ARTEMIS: Spatial and temporal distribution and constraints on species and source locations, *J. Geophys. Res.*, *117*, E06006, doi:10.1029/2012JE004107.
- Halekas, J. S., A. R. Poppe, G. T. Delory, M. Sarantos, and J. P. McFadden (2013), Utilizing ARTEMIS pickup ion observations to place constraints on the lunar atmosphere, *J. Geophys. Res. Planets*, *118*, 1–8, doi:10.1029/2012JE004292.
- Harada, Y., S. Machinda, J. S. Halekas, A. R. Poppe, and J. P. McFadden (2013), ARTEMIS observations of lunar dayside plasma in the terrestrial magnetotail lobe, *J. Geophys. Res. Space Physics*, *118*, 1–8, doi:10.1002/jgra.50296.
- Hodges, R. R. (1975), Formation of the lunar atmosphere, *Moon*, *14*, 139–157.
- Hodges, R. R. (1980), Lunar cold traps and their influence on argon-40, *Proc. Lunar Planet. Sci. Conf. 11th*, *11*, 2463–2477.
- Hodges, R. R., J. H. Hoffman, F. S. Johnson, and D. E. Evans (1973), Composition and dynamics of lunar atmosphere, *Proc. 4th Lunar Sci. Conf.*, *3*, 2855–2864.
- Hoffman, J. H., R. R. Hodges Jr., F. S. Johnson, and D. E. Evans (1973), Lunar atmospheric composition results from Apollo 17, *Proc. 4th Lunar Sci. Conf.*, *3*, 2865–2875.
- Huebner, W. F., J. J. Keady, and S. P. Lyon (1992), Solar photo rates for planetary atmospheres and atmospheric pollutants, *Astrophys. Space Sci.*, *195*, 1–294.
- Ip, W.-H. (1996), Europa's oxygen exosphere and its magnetospheric interaction, *Icarus*, *120*, 317–325.
- Ip, W.-H., D. J. Williams, R. W. McEntire, and B. H. Mauk (1998), Ion sputtering and surface erosion at Europa, *Geophys. Res. Lett.*, *25*(6), 829–832.
- Johnson, R. E., and R. Baragiola (1991), Lunar surface: Sputtering and secondary ion mass spectrometry, *Geophys. Res. Lett.*, *18*(11), 2169–2172.
- Killen, R. M. (2002), Source and maintenance of the argon atmospheres of Mercury and the Moon, *Meteorit. Planet. Sci.*, *37*, 1223–1231.
- Killen, R. M., M. Sarantos, A. E. Potter, and P. Reiff (2004), Source rate and ion recycling rates for Na and K in Mercury's atmosphere, *Icarus*, *171*, 1–19.
- Killen, R. M., D. M. Hurley, and W. M. Farrell (2012), The effect on the lunar exosphere of a coronal mass ejection passage, *J. Geophys. Res.*, *117*, E00K02, doi:10.1029/2011JE004011.
- Leblanc, F., D. Delcourt, and R. E. Johnson (2003), Mercury's sodium exosphere: Magnetospheric ion recycling, *J. Geophys. Res.*, *108*(E12), 5136, doi:10.1029/2003JE002151.
- Luhmann, J. G., T.-L. Zhang, S. M. Petrinec, C. T. Russell, P. Gazis, and A. Barnes (1993), Solar cycle 21 effects on the interplanetary magnetic field and related parameters at 0.7 and 1.0 AU, *J. Geophys. Res.*, *98*(A4), 5559–5572.
- Mall, U., et al. (1998), Direct observation of lunar pick-up ions near the Moon, *Geophys. Res. Lett.*, *25*(20), 3799–3802.
- Morgan, T. H., and R. M. Killen (1997), A non-stoichiometric model of the composition of the atmospheres of Mercury and the Moon, *Planet. Space Sci.*, *45*(1), 81–94.
- O'Brien, T. P., S. M. Thompson, and R. L. McPherron (2002), Steady magnetospheric convection: Statistical signatures in the solar wind and AE, *Geophys. Res. Lett.*, *29*(7), 34-1–34-4, doi:10.1029/2001GL014641.
- Poppe, A., and M. Horányi (2010), Simulations of the photoelectron sheath and dust levitation on the lunar surface, *J. Geophys. Res.*, *115*, A08106, doi:10.1029/2010JA015286.
- Poppe, A., J. S. Halekas, and M. Horányi (2011), Negative potentials above the day-side lunar surface in the terrestrial plasma sheet: Evidence of non-monotonic potentials, *Geophys. Res. Lett.*, *38*, L02103, doi:10.1029/2010GL046119.
- Poppe, A. R., J. S. Halekas, G. T. Delory, W. M. Farrell, V. Angelopoulos, J. P. McFadden, J. W. Bonnell, and R. E. Ergun (2012a), A comparison of ARTEMIS observations and particle-in-cell modeling of the lunar photoelectron sheath in the terrestrial magnetotail, *Geophys. Res. Lett.*, *39*, L01102, doi:10.1029/2011GL050321.
- Poppe, A. R., R. Samad, J. S. Halekas, M. Sarantos, G. T. Delory, W. M. Farrell, V. Angelopoulos, and J. P. McFadden (2012b), ARTEMIS observations of lunar pick-up ions in the terrestrial magnetotail, *Geophys. Res. Lett.*, *39*, L17104, doi:10.1029/2012GL052909.
- Poppe, A. R., J. S. Halekas, R. Samad, M. Sarantos, and G. T. Delory (2013), Model-based constraints on the lunar exosphere derived from ARTEMIS pick-up ion observations in the terrestrial magnetotail, *J. Geophys. Res. Planets*, *118*, 1–13, doi:10.1002/jgre.20090.
- Potter, A. E., and T. H. Morgan (1998), Coronagraphic observations of the lunar sodium exosphere near the lunar surface, *J. Geophys. Res.*, *103*(E4), 8581–8586.
- Potter, A. E., R. M. Killen, and T. H. Morgan (2000), Variation of lunar sodium during passage of the Moon through the Earth's magnetotail, *J. Geophys. Res.*, *105*(E6), 15,073–15,084.
- Reasoner, D. L., and W. J. Burke (1972), Direct observation of the lunar photoelectron layer, *Proc. 3rd Lunar Sci. Conf.*, *3*, 2639–2654.
- Roussos, E., N. Krupp, H. Krüger, and G. H. Jones (2010), Surface charging of Saturn's plasma-absorbing moons, *J. Geophys. Res.*, *115*, A08225, doi:10.1029/2010JA015525.
- Sarantos, M., R. M. Killen, A. Surjalal Sharma, and J. A. Slavin (2008), Influence of plasma ions on source rates for the lunar exosphere during passage through the Earth's magnetosphere, *Geophys. Res. Lett.*, *35*, L04105, doi:10.1029/2007GL032310.
- Sarantos, M., R. E. Hartle, R. M. Killen, Y. Saito, J. A. Slavin, and A. Gloer (2012a), Flux estimates of ions from the lunar exosphere, *Geophys. Res. Lett.*, *39*, L13101, doi:10.1029/2012GL052001.
- Sarantos, M., R. M. Killen, D. A. Glenar, M. Benna, and T. J. Stubbs (2012b), Metallic species, oxygen and silicon in the lunar exosphere: Upper limits and prospects for LADEE measurements, *J. Geophys. Res.*, *117*, A03103, doi:10.1029/2011JA017044.
- Schultz, P. H., et al. (2010), The LCROSS cratering experiment, *Science*, *330*(330), 468–472.
- Sergeev, V. A., R. J. Pellinen, and T. I. Pulkkinen (1996), Steady magnetospheric convection: A review of recent results, *Space Sci. Rev.*, *75*, 551–604.
- Sibeck, D. G., et al. (2011), ARTEMIS science objectives, *Space Sci. Rev.*, *165*(1–4), 59–91.
- Sigmund, P. (1969), Theory of sputtering. I. Sputtering yield of amorphous and polycrystalline targets, *Phys. Rev.*, *184*, 383–416.
- Stern, S. A. (1999), The Lunar Atmosphere: History, status, current problems, and context, *Rev. Geophys.*, *37*(4), 453–491.
- Stern, S. A., K. D. Retherford, C. C. Tsang, P. D. Feldman, W. Pryor, and G. R. Gladstone (2012), Lunar atmospheric helium detections by the LAMP UV spectrograph on the Lunar Reconnaissance Orbiter, *Geophys. Res. Lett.*, *39*, L12202, doi:10.1029/2012GL051797.
- Tanaka, T., et al. (2009), First in situ observation of the Moon-originating ions in the Earth's Magnetosphere by MAP-PACE on SELENE (KAGUYA), *Geophys. Res. Lett.*, *36*, L22106, doi:10.1029/2009GL040682.
- Troshichev, O., S. Kokubun, Y. Kamide, A. Nishida, T. Mukai, and T. Yamamoto (1999), Convection in the distant magnetotail under extremely quiet and weakly disturbed conditions, *J. Geophys. Res.*, *104*(A5), 10,249–10,263.
- Wang, X.-D., et al. (2011), Detection of  $m/q=2$  pickup ions in the plasma environment of the Moon: The trace of exospheric  $H_2^+$ , *Geophys. Res. Lett.*, *38*, L14204, doi:10.1029/2011GL047488.
- Wurz, P., U. Rohner, J. A. Whitby, C. Kolb, H. Lammer, P. Dobnikar, and J. A. Martín-Fernández (2007), The lunar exosphere: The sputtering contribution, *Icarus*, *191*, 486–496.
- Wurz, P., J. A. Whitby, U. Rohner, J. A. Martín-Fernández, H. Lammer, and C. Kolb (2010), Self-consistent modelling of Mercury's exosphere by sputtering micro-meteorite impact and photon-stimulated desorption, *Planet. Space Sci.*, *58*, 1599–1616.
- Yakshinskiy, B. V., and T. E. Madey (1999), Photon-stimulated desorption as a substantial source of sodium in the lunar atmosphere, *Nature*, *400*, 642–644.
- Yokota, S., et al. (2009), First direct detection of ions originating from the Moon by MAP-PACE IMA onboard SELENE (KAGUYA), *Geophys. Res. Lett.*, *36*, L11201, doi:10.1029/2009GL038185.
- Zimmerman, M. I., W. M. Farrell, T. J. Stubbs, J. S. Halekas, and T. L. Jackson (2011), Solar wind access to lunar polar craters: Feedback between surface charging and plasma expansion, *Geophys. Res. Lett.*, *38*, L19202, doi:10.1029/2011GL048880.
- Zimmerman, M. I., T. L. Jackson, W. M. Farrell, and T. J. Stubbs (2012), Plasma wake simulations and object charging in a shadowed lunar crater during a solar storm, *J. Geophys. Res.*, *117*, E00K03, doi:10.1029/2012JE004094.